

Vision-Based Sensor for Real-Time Measuring of Surface Traction Fields



Kazuto Kamiyama, Kevin Vlack, Terukazu Mizota, Hiroyuki Kajimoto, Naoki Kawakami, and Susumu Tachi
University of Tokyo

The desire to reproduce and expand the human senses drives innovations in sensor technology. Conversely, human-interface research aims to allow people to interact with machines as if they were natural objects in a cybernetic, human-oriented way. We wish to unite the two paradigms with a haptic sensor as versatile as the sense of touch and developed for a dual purpose: to improve the robotic capability to interact with the physical world, and to improve the human capability to interact with the virtual world for emerging applications with a heightened sense of presence.

By measuring a surface traction field, the GelForce tactile sensor can represent the magnitude and direction of force applied to the skin's surface.

When force is applied to the skin's surface, the human sense of touch detects not only magnitude but also direction of force distributed over a surface. We obtain rich tactile information with a robustness that is difficult to emulate through technology. The difficulty lies in obtaining vector information with both high speed and high density. We're developing a type of tactile sensor that uses computer vision to achieve this goal. We designed a sensor, dubbed *GelForce*, that acts as a practical tool in both conventional and novel desktop applications using common consumer hardware.

Surface traction field measurement

The spatial characteristics of objects in contact are encoded in the human somatosensory system by a dense population of subcutaneous mechanoreceptors. Neural activity is triggered by deformation, and is sensitive to direction and orientation of applied stimuli. Generally speaking, we perceive a *traction field*, or a 3D force field defined over a 2D surface. Measuring such a field is a central concern for endowing a human-like sense of touch to mechanical devices.

Elastostatic theory

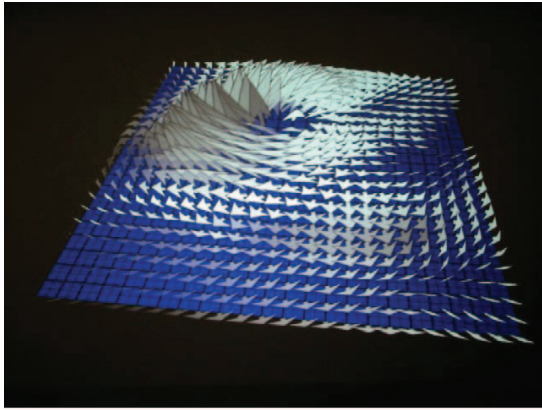
The principles of our sensor are rooted in elasticity theory (see Hetnarski and Ignaczak¹ for an excellent discourse on the subject). We adopt a standard Cartesian coordinate system in \mathfrak{R}^3 , where the set of vectors $\{\mathbf{e}_i\} = \{\mathbf{e}_1, \mathbf{e}_2, \mathbf{e}_3\}$ and origin $\mathbf{0}$ represent an orthonormal basis, with $x_i = \mathbf{x} \cdot \mathbf{e}_i$ giving the coordinates for points \mathbf{x} in \mathfrak{R}^3 . By convention, we define an elastic body B with boundary ∂B as a set of elements \mathbf{x} with a one-to-one correspondence with points in physical space. We define a deformation of B as a uniquely invertible map κ of B onto $\kappa(B)$. A vector field $\mathbf{u}(\mathbf{x}, t)$ representing the displacement of B to a new configuration describes the motion, which we define as

$$\mathbf{u}(\mathbf{x}, t) = \kappa(\mathbf{x}, t) - \mathbf{x} \quad (1)$$

where $\kappa(\mathbf{x}, t)$ is the point occupied by \mathbf{x} at time t . We associate velocity with $\dot{\mathbf{u}}$ and acceleration with $\ddot{\mathbf{u}}$. For a time-independent equilibrium state where $\ddot{\mathbf{u}}(\mathbf{x}, t) = \ddot{\mathbf{u}}(\mathbf{x}) = 0$, elastostatic theory dictates admissibility conditions for $\mathbf{u}(\mathbf{x})$ and a 3×3 stress tensor field $\mathbf{S}(\mathbf{x})$ for all points $\mathbf{x} \in B$.

For practical problems with specified boundary conditions in B , the remaining effort is obtaining continuous and self-equilibrated solutions for $[\mathbf{u}, \mathbf{S}]$ in B . An example naturally arising in haptics is to solve for $\mathbf{u}(B)$ given a surface traction field $\mathbf{s}(\partial B)$ or a stress vector field $\mathbf{s}(\mathbf{x}) = \mathbf{S}(\mathbf{x})\mathbf{n}(\mathbf{x})$ for all points $\mathbf{x} \in \partial B$, where $\mathbf{n}(\mathbf{x})$ is the outward normal vector at \mathbf{x} . Figure 1 shows an example traction field on a plane with $\mathbf{n}(\mathbf{x}) = (0, 0, 1)$.

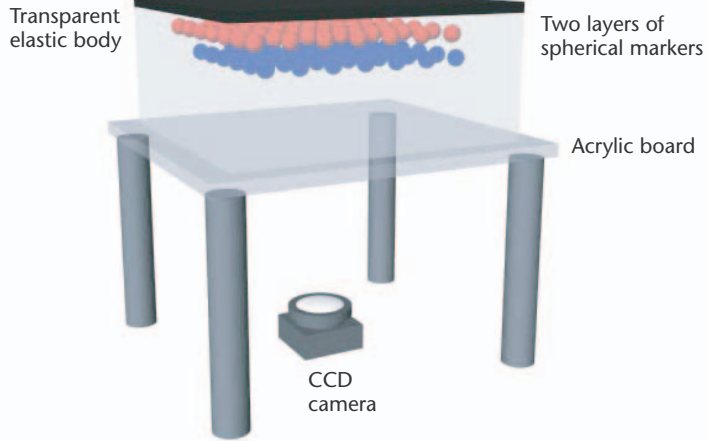
Finding the corresponding solution $[\mathbf{u}, \mathbf{S}]$ is laborious in general. To simplify the problem, we assume the elastic medium is linear, isotropic, and homogeneous. These are common assumptions because they closely approximate the actual properties of many engineering materials, and an analytical solution is often intractable without them.



1 Traction fields measured in real time.

System design

The body B of our sensor, illustrated in Figure 2, is a $10 \times 10 \times 4$ -cm rectangular block of transparent silicone rubber fixed by an acrylic board. We printed a collection of colored markers, 0.6 mm in diameter, inside the elastic body at approximately 3-mm intervals. We mounted a color charge-coupled device (CCD) camera 15 cm below the markers, pointed upward. To control the lighting conditions, we placed an opaque black layer of identical elastic material over the body's surface and illuminated the body's interior with white light-emitting diodes (LEDs).



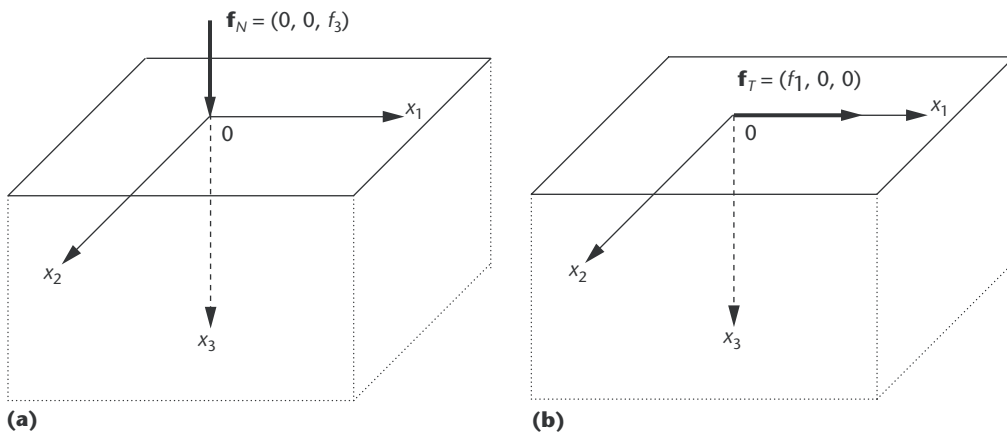
2 Basic schematic of proposed sensor.

When we apply force to the topmost planar surface ∂B , the camera measures the markers' displacement. The rubber has low hysteresis (energy loss) and quickly relaxes to its original configuration when force is released. Thus, we can effectively treat the body as a static infinite semispace with only a modest accuracy loss.

Elastic semispace problem

Consider the linear elastic state in a homogeneous isotropic semispace B defined by the inequalities $|x_1| < \infty$, $|x_2| < \infty$, and $0 < x_3 < \infty$, subject to a traction field $\mathbf{s}(\mathbf{x})$ on boundary $\partial B = \{\mathbf{x} : x_3 = 0\}$, with the x_3 axis defined perpendicular to the surface and directed toward its interior. We seek an admissible solution for $[\mathbf{u}, \mathbf{S}]$ that is continuous over B . We first consider two elemental cases of the Green's functions for a point force applied at origin 0. The proofs are extensive and thus omitted for brevity (see Hetnarski and Ignaczak¹ for a rigorous discussion).

The first case is a normal point force $\mathbf{f}_N = (0, 0, f_3)$, as shown in Figure 3a. We obtain the resulting displacement vector field $\mathbf{u}_N(\mathbf{x})$ for internal points $\mathbf{x} \in B$ from the Boussinesq solution



3 Two cases of point force: (a) Boussinesq problem of normal point force; (b) Cerruti problem of tangential point force.

$$\begin{pmatrix} u_1 \\ u_2 \\ u_3 \end{pmatrix}_N = f_3 \frac{(1+\nu)}{2\pi ER} \begin{pmatrix} \frac{x_1 x_3}{R^2} - \frac{(1-2\nu)x_1}{R+x_3} \\ \frac{x_2 x_3}{R^2} - \frac{(1-2\nu)x_2}{R+x_3} \\ \frac{x_3^2}{R^2} + (2-2\nu) \end{pmatrix} \quad (2)$$

where

$$R = \sqrt{x_1^2 + x_2^2 + x_3^2} > 0$$

is the distance of \mathbf{x} from $\mathbf{0}$.

The first elasticity constant in Equation 2 is Young’s modulus $E > 0$ with units in Pascals, characterizing stiffness. The elastic material we use is a stiff silicone rubber with a high E value, so for a wide range of applied force, any elastic displacement is small relative to the body’s total size.

The second constant is Poisson’s ratio $-1 \leq \nu \leq 1/2$, characterizing compressibility. Very compressible materials such as cork have a value close to 0, and nearly incompressible elastomers, such as silicone, have a ratio close to 1/2. Some synthetic materials have molecular lattices that effectively expand under tension, granting a negative value.

The second case is a tangential point force $\mathbf{f}_{T1} = (f_1, 0, 0)$, as Figure 3b shows. Here, we obtain the resulting displacement vector field $\mathbf{u}_{T1}(\mathbf{x})$ from the Cerruti solution

$$\begin{pmatrix} u_1 \\ u_2 \\ u_3 \end{pmatrix}_{T1} = f_1 \frac{(1+\nu)}{2\pi ER} \begin{pmatrix} \frac{R^2 + x_1^2}{R^2} + (1-2\nu) \frac{R^2 + Rx_3 + x_1^2}{(R+x_3)^2} \\ \frac{x_1 x_2}{R^2} - (1-2\nu) \frac{x_1 x_2}{R(R+x_3)^2} \\ \frac{x_1 x_3}{R^2} + (1-2\nu) \frac{x_1}{R^2(R+x_3)} \end{pmatrix} \quad (3)$$

where R is defined as it is in Equation 2. Clearly, we might also find \mathbf{u}_{T2} for a tangential force $\mathbf{f}_{T2} = (0, f_2, 0)$ by interchanging x_1 and x_2 as well as u_1 and u_2 in Equation 3.

Because we assume the elastic medium is linear, given an arbitrary point force $\mathbf{f} = (f_1, f_2, f_3)$, by superposition we can gather the solutions for \mathbf{u}_{T1} , \mathbf{u}_{T2} , and \mathbf{u}_N into matrix form $\mathbf{u}(\mathbf{x}) = \mathbf{H}(\mathbf{x})\mathbf{f}$, where $\mathbf{H}(\mathbf{x})$ is a 3×3 tensor field dependent entirely on the position \mathbf{x} . We obtain a traction vector field by parameterizing stress vectors $\mathbf{s}(v, w)$ over a domain boundary map $\Omega: \Omega \times \mathfrak{R}^2 \rightarrow \partial B$ and compute the displacement field for any interior point $\mathbf{x} \in B$ from the formula

$$\mathbf{u}(\mathbf{x}) = \int_{\Omega} \mathbf{H}(\mathbf{x} - \Omega(v, w)) \mathbf{s}(v, w) dv dw \quad (4)$$

To formulate the extended semispace problem’s discrete solution, we define a *discrete traction field* $\Phi = [\{\mathbf{f}_1, \mathbf{f}_2, \dots, \mathbf{f}_n\}, \{\xi_1, \xi_2, \dots, \xi_n\}]$ as a set of n distinct impulsive point forces \mathbf{f}_i and their respective positions $\xi_i \in \partial B$,

which can be chosen freely. Equation 4 then takes the form

$$\mathbf{u}(\mathbf{x}) = \sum_{i=1}^n \mathbf{H}(\mathbf{x} - \xi_i) \mathbf{f}_i$$

For a set of m distinct sample points $\{\mathbf{x}_1, \mathbf{x}_2, \dots, \mathbf{x}_m\}$, where $\mathbf{x}_i \in B$, convoluting over \mathbf{x} and ξ lets us represent the tensor field $\mathbf{H}(\mathbf{x})$ by a constant $3m \times 3n$ block matrix $\bar{\mathbf{H}}$ such that

$$\mathbf{u}(\mathbf{x}_j) = \bar{\mathbf{H}}_{i,j} \mathbf{f}_i \quad (5)$$

where $\bar{\mathbf{H}}_{i,j} = \mathbf{H}(\mathbf{x}_j - \xi_i)$

Because we can only measure $\mathbf{u}(\mathbf{x})$ with a camera, we seek the inverse problem—namely, to derive a discrete traction field $\mathbf{f}(\mathbf{x})$ given a displacement field $\mathbf{u}(\mathbf{x})$. So, for $m \geq n$, we obtain the $3n \times 3m$ block pseudoinverse matrix \mathbf{Q} through a standard linear squares scheme, such as the normal equations method:

$$\begin{aligned} \bar{\mathbf{H}}^T \mathbf{u} &= (\bar{\mathbf{H}}^T \bar{\mathbf{H}}) \mathbf{f} \\ [(\bar{\mathbf{H}}^T \bar{\mathbf{H}})^{-1} \bar{\mathbf{H}}^T] \mathbf{u} &= \mathbf{f} \\ \mathbf{Q} \mathbf{u} &= \mathbf{f} \end{aligned}$$

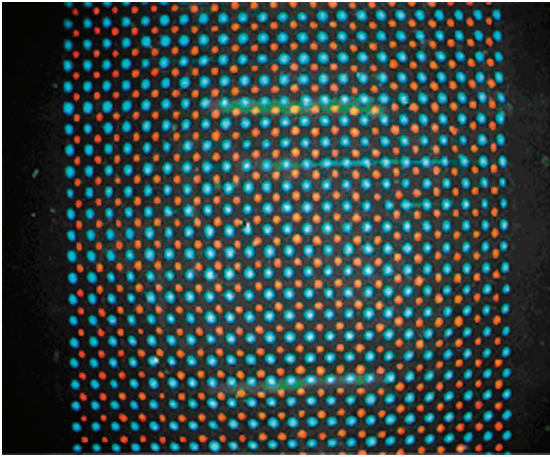
The matrix $\bar{\mathbf{H}}$ is constant, and well conditioned for appropriate choices of \mathbf{x} and ξ . Moreover, we can accurately compute the constant \mathbf{Q} using a Cholesky factorization in a precomputation phase and then apply it online at every frame to compute a discrete traction field with a single matrix-vector multiplication.

Measuring displacement information

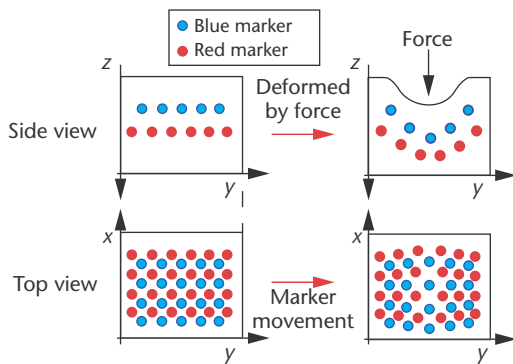
Researchers have developed a wide variety of methods for acquiring force information as a distribution. Examples include the strain gauge and recent devices based on piezoelectric elements (see the “Related Work” sidebar). To circumvent circuitry-related complications for large-scale, high-density sensing, we adopted an approach based on computer vision, which has grown increasingly popular in robotics as the cost and size of high-quality imaging systems has decreased. Issues concerning linear perspective and lens distortion² are discussed in detail elsewhere, and for now we shall assume they are properly accounted for.

Single marker displacement. We use a fast and simple approach to measure the planar movement of the circular markers described earlier. Figure 4 shows an image captured by the CCD camera and sent directly to a PC. The captured area’s size is 100×75 mm, so one pixel of the 640×480 image roughly corresponds to a 0.15-mm square. To reduce background noise effects, we applied a threshold to the image’s color channels to accentuate the marker arrangement topology. This is analogous to raising the water level to segment a hilly landscape into a chain of islands.

To measure marker displacement within the captured image, we decompose the image into small independent cells. We initially detect each marker’s location through a windowed autocorrelation technique and then create a bounding box M_i large enough to contain the marker



4 CCD camera image of interior elastic body.



5 Representing depth information through color.

for all of its expected displacement range. Because the rubber is stiff and the deformation is mostly reversible, this amounts to only a few pixels in each direction, even for a wide range of applied force. To compute the position \mathbf{x}_i in M_i , we apply a standard discrete center of mass calculation over all pixels \mathbf{p}

$$\mathbf{X}_i = \frac{\sum_{\mathbf{p} \in M_i} \mathbf{p} \eta(\mathbf{p})}{\sum_{\mathbf{p} \in M_i} \eta(\mathbf{p})}$$

where $\eta(\mathbf{p})$ denotes the image intensity at pixel \mathbf{p} in the corresponding color channel. During a calibration stage when no force is applied, we store the initial marker positions \mathbf{x} . Applying force deforms the positions to $\kappa(\mathbf{x})$, and we compute the displacement $\mathbf{u}(\mathbf{x})$ using Equation 1. We've found empirically that we can calculate the position to a precision of less than 0.1 pixels, which corresponds to approximately 15 microns in the xy -plane.

Depth information through color. Clearly, the third component of \mathbf{u} in Equation 1 is unobtainable because a pixel \mathbf{p} has only two components, corresponding to row and column. However, elastic boundary value problems are generally invertible as long as there are

Related Work

Nearly all existing force sensors belong to one of two categories.^{1,2} The first measures a force vector at a single point; the second measures a distribution of forces, but only the forces' magnitude, not their direction. Few sensors can measure force as a vector distribution, or *traction field*. Most current sensors use a sensing unit in which mechanical pressure causes variances in electric resistance or capacitance.^{1,3,4} These sensors require complex wiring and a large sensor unit to measure dense traction fields. This is especially problematic when the sensors are integrated into a compact mechanism such as a robotic hand or a desktop accessory.

An alternative force-sensing method uses optics. Optical sensors require much less circuitry and allow dense measurement at low cost. However, few reported optical sensors measure traction fields. Ohoka et al. developed a sensor using an elastic sheet and a collection of pyramidal projections arranged in a transparent board parallel to the sheet.⁵ The sensor measures a traction field by monitoring the projections, but for it to properly measure force, the projections must be adjusted precisely.

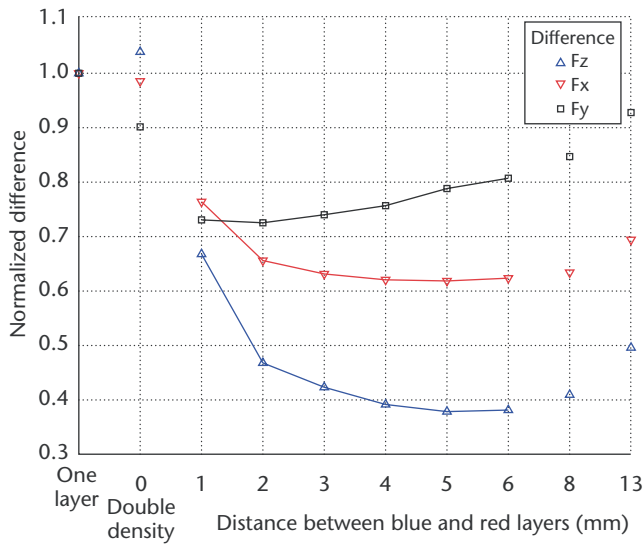
Ferrier and Brockett proposed a shape sensor, coincidentally with a system design similar to ours, that tracks dots on an elastic material to compute the 3D configuration of a fingertip-shaped elastic membrane.² Their measurement approach is robust and reportedly performed at interactive refresh rates for problem domains with dozens of vector elements.

References

1. R.S. Fearing, "Using a Cylindrical Tactile Sensor for Determining Curvature," *IEEE Trans. Robotics and Automation*, vol. 7, no. 6, 1991, pp. 806-817.
2. N.J. Ferrier and R.W. Brockett, "Reconstructing the Shape of a Deformable Membrane from Image Data," *Int'l J. Robotics Research*, vol. 19, no. 9, 2000, pp. 795-816.
3. J.G. Silva, A.A. Carvalho, and D.D. Silva, "A Strain Gauge Tactile Sensor for Finger-Mounted Applications," *IEEE Trans. Instrumentation and Measurement*, vol. 51, no. 1, 1991, pp. 18-22.
4. D.T.V. Pawluk et al., "Distributed Pressure Sensor for Biomechanical Measurements," *J. Biomechanical Eng., Trans. ASME*, vol. 120, no. 2, 1998, pp. 302-305.
5. M. Ohoka et al., "Data Conversion Capability of Optical Tactile Sensor Featuring an Array of Pyramidal Projections," *Proc. IEEE Conf. Multisensor Fusion and Integration for Intelligent Systems*, IEEE Press, 1996, pp. 573-580.

at least as many independent equations as there are unknown variables.³ No definitive correspondence between markers and force vectors exists, so even though we obtain only 2D displacement information, we can still solve the discrete semispace problem for n 3D force vectors as long as the number of sample points m is at least $3n/2$.

Although the elastostatic theory guarantees invertibility, no such assurance regarding the problem's stability exists when complete displacement information is unknown. Indeed, as we show in the next section, our method's accuracy experiences a marked degradation when there is no depth information in the measured displacement. We therefore use two layers of markers at separate depths, interspersing them to avoid occlusion, as Figure 5 illustrates. We distinguish the layers by color, in this case red and blue, so by separating the color chan-



6 Simulated errors versus layer separation distance. Fx, Fy, and Fz depict the errors for each measured force component.

nels in an RGB stream, we obtain two planar displacement distributions in each image. In Figure 5, the blue marker layer is at $x_3 = 6.0$ mm, and the red layer is at $x_3 = 8.0$ mm. It follows from Equations 2 and 3 that for a point force at the origin, the displacement of internal points diminishes on the order of $o(R^{-1})$. At small depths the difference is substantial. This added information can compensate for the dimension lost using a single camera.

Evaluation experiments

Measuring traction fields optically is a relatively new concept, and there are concerns about the accuracy and effectiveness of the method. In contrast to most conventional mechanical sensors, there is no obvious input-output relationship between the captured image and the computed force field. We therefore assess the performance of our optical traction field sensor with a few evaluation experiments.

Force vector evaluation

We first evaluated the effectiveness of the two layers of markers and the influence of distance between the blue and red layers using a simulated model of the sensor with the same specifications as the actual system. We chose a discrete computed traction field Φ as an $n = 24 \times 24$ square grid of force vectors centered at the origin. We then simulated an applied discrete traction field $\hat{\Phi}$ on the surface with 100 force vectors arranged in a square given by

$$\left\{ \begin{array}{l} \hat{f}_{ij} = (0, 50, 100) \\ \xi_{ij} = (3i, 3j, 0) \end{array} : i, j = \{-5, -4, \dots, 3, 4\} \right\}$$

with units properly scaled to the image size.

We investigated the effect of the two layers by comparing Φ and $\hat{\Phi}$. Iterating the simulation let us systematically change the given distance between the two

layers. We simulated $m = 576$ red + 576 blue internal markers with positions Ψ obtained from an actual CCD camera image. Given applied traction field $\hat{\Phi}$, we used Equation 5 to calculate the theoretical displacement vector field $u(\Psi)$ for the markers and mapped it to account for linear perspective. We multiplied the result by the $2m \times 3n$ pseudoinverse matrix Q to obtain Φ .

Figure 6 shows the mean difference between the individual vectors f_i in Φ and \hat{f}_i in $\hat{\Phi}$ for each component. On the horizontal axis, from left to right, the mean values are for only the blue layer, the blue and red marker layers at the same depth, then each case with an interlayer distance between 1 and 6 mm, then 8 and 13 mm. Having the blue and red layers located at the same depth is equivalent to doubling the density of sampling points at only one layer. Because we scale the computed field Φ arbitrarily, results are normalized with respect to the absolute error obtained by a single layer of blue markers. Although the average of the difference is almost the same in the first two cases, as the layers separate, the mean difference decreases. However, this trend bottoms out, and the mean difference increases with additional separation. This conclusion suggests that the proposed method is most accurate when the difference between the two marker layers is 2 or 3 mm, the distance adopted in our prototype.

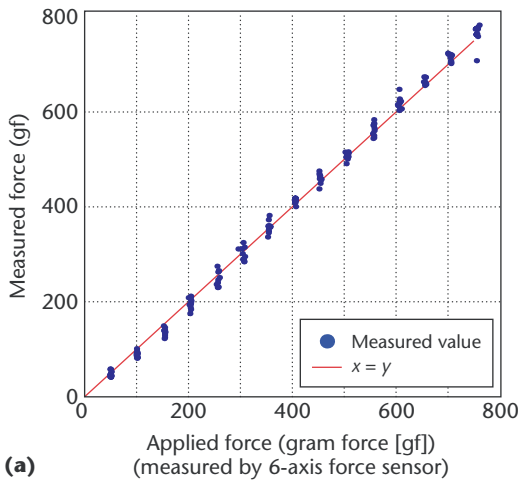
We then evaluated the resolution of force magnitude and direction. We applied an actual traction field using a probe with a 5-mm diameter hemispherical contact site. Summating each force vector in the computed Φ gives us a total computed force f . By comparing f with the total applied force \hat{f} measured by a separate 6-axis force sensor controlled by an xyz-stage, we examine the resolution and linearity of the measurement Φ .

First, we investigated the magnitude of the computed force f . We increased the applied normal force \hat{f} from 0 to 750 gram force (gf) by 50 gf increments and recorded the computed force over 10 trials. Figure 7a shows the result. The straight plot indicates that the sensor can sufficiently measure the force linearly with a magnitude resolution of about 30 gf. We expect that using a less stiff material might further improve the result.

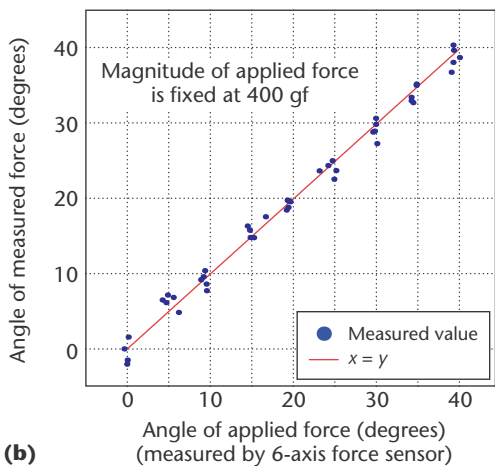
Next, we estimated the force’s angle resolution. Using the same hemispherical probe, we fixed the magnitude of the applied force \hat{f} at 400 gf and applied the force at a variable angle with respect to the surface normal, changing from 0 to 45 by 5-degree increments. The probe’s base plane remains parallel to the xy-plane. Figure 7b shows the result. As the figure shows, the proposed force sensor measures the angle of force precisely and linearly. The graph’s data spread shows that the measured force’s angle resolution is about 5 degrees.

The proposed force sensor calculates force using a pseudoinverse matrix, so the computed result at each point includes an error that is distributed around its neighbors. We investigated this error’s effects on spatial resolution. For simplicity, for each force vector we considered only the normal component f_N and tangential component f_T . The evaluation used an applied traction field from force applied at a certain point on the surface.

However, because the sampling interval isn’t fine enough to estimate the distributed error, we adopted the following procedure. We selected two adjacent mea-



(a)



(b)

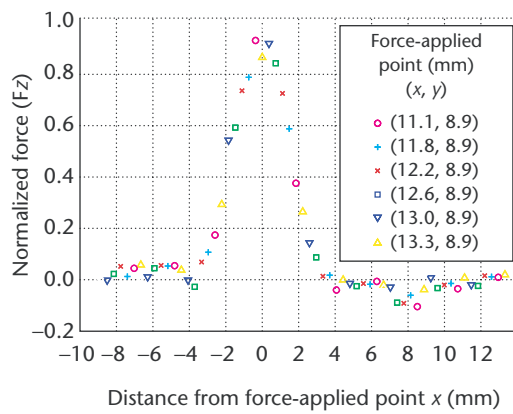
7 Relation between applied and measured force for (a) z-direction and (b) angle from the surface.

surement points, (f_i, x_i) and (f_j, x_j) , from the computed traction field Φ , subdivided the distance between them into n points, and applied a given perpendicular force \hat{f}_N at each point. Then, we computed force vectors \mathbf{f}_N at each point, regarding each point as the origin. We repeated this procedure as we increased the density of sampling points in Φ and then derived the spatial resolution of Φ from the obtained force distribution's width.

Figure 8 shows the result, with the horizontal axis representing the distance from each origin, and the vertical axis representing the normal component of the measured force vector \mathbf{f} . We normalize the vertical axis value using the maximum value among the acquired data. The magnitude of normal applied force \hat{f}_N is fixed at 200 gf and the adjacent measurement points are at the center of the area in which we acquire force distribution. The actual measurement interval is 2.2 mm, and we subdivide adjacent points into 0.37-mm intervals. Half of the width, in effect the spatial resolution of forces in Φ , is about 4 mm.

Performance evaluation

The core motivation of GelForce is to measure a large-scale and high-density surface traction field in real time, so a few words regarding performance are in order.



8 Normal component of measured force at high-density sampling when we apply point force.

Table 1 summarizes the prototype's specifications and execution times.

Applications

As computing hardware improves, many applications are emerging that induce a heightened sense of presence for the user. Accordingly, we can expect an increased demand for input and control devices with high bandwidth and rich geometrical structure.

Interactive digital art

Because the GelForce sensor measures dense traction fields in real time, it shows promise for novel interactive digital artwork. To assess the computed field's geometrical structure, we implemented several visualizations in an application called GelVis using various graphics hardware acceleration techniques to visualize vector fields, contour plots, and spline surfaces. Applying force to the surface let us easily achieve sophisticated visual effects, such as those in Figure 9.

We confirmed many of the force vector distribution interface's novel capabilities through visualization. For example, when we slid a finger along the sensor's surface, the force vector field followed the movement smoothly, with the distribution's leading end correctly pointing parallel to the surface. When we applied torque to the sensor's surface, the traction field indicated a curling distribution. Pressing on the elastic body with various intensities, ranging from a gentle tap to a full-strength press, causes the displayed arrows to scale correctly along the complete range of applied force.

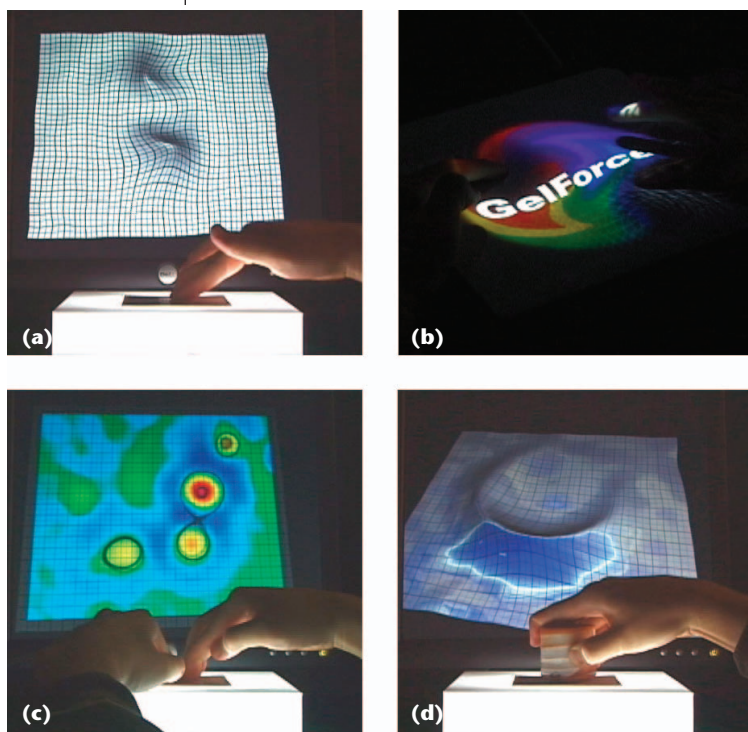
Universal computer interface

The developed sensor is inexpensive to manufacture and easy to use. With the continual improvement of CPU and GPU technology, novel uses for high-bandwidth traction field sensing in image processing, animation, virtual reality, music, and computer entertainment will soon become mainstream.

Most conventional interfaces, such as the keyboard or pointer device, rely on applied force sensors. Force input devices can be classified by measured value and measured region dimensions. For example, a standard joystick measures a 2D force vector at a 0D point, and a

Table 1. Prototype system specifications and execution times.

Feature	Description
Size	10 × 10 × 15 cm
Elastic body	Silicone rubber, 10 × 10 × 4 cm (Young's modulus $E \approx 1.8 \times 10^4$ Pa, Poisson's ratio $\nu \approx 0.49$)
Markers	Two 24 × 24 grids at 3-mm intervals Depth: (blue) 6 mm, (red) 8 mm
Traction field	24 × 24 regular grid of 3D vectors
Resolution	Magnitude: 30 gf Direction: 5 degrees Spatial: 4 mm
Camera	Point Grey Research Streaming Dragonfly (640 × 480 RGB, 30 frames per second)
CPU	Intel Pentium 4 HT, 2.6 GHz
Implementation	Intel C/C++ Compiler 8.0 Intel Math Kernel Library 6.1
Precomputation	Normal equations to compute $1,728 \times 2,304$ pseudoinverse: 8.5 seconds
Time per frame	Marker tracking: 1.07 ms Traction computation: 11.5 ms Frame rate restricted by camera



9 GelVis snapshots: (a) deformed surface with multiple contact points, (b) overhead projection onto sensor surface, (c) contour plot of measured force magnitude, and (d) complex traction field with a curved object.

pressure-pad³ measures 1D force magnitude over a 2D surface. Generally speaking, sensors with higher dimensions of either measured value or region are more universal. That is, any device that can measure a 3D vector can obviously measure a 2D vector or a 1D scalar, and likewise for measurement region.

As such, we wish to exploit the universality of traction fields to support existing applications as well. Standard techniques, such as spline interpolation and flow

analysis,⁴ are useful for accurately extracting critical points, such as concentrated forces or vortices, that can be used for familiar tasks such as point-based control, affine transformations, and text input.

Robotic sense of touch

A traction field sensor can endow a robotic fingertip with a lifelike sense of touch. Simple tasks, such as picking up an egg, depend on feeling the weight of an object not only by muscle contraction but also by force parallel to the skin. Adjusting the proportion of perpendicular and parallel force lets humans grasp fragile objects safely. Similarly, to operate dexterously, robots must sense both the grasping and the friction force on the fingertip. With appropriate Green's functions, we can use the principles behind the GelForce sensor to measure traction fields for an arbitrary shape, such as a fingertip, so it can easily be mounted on a robot hand. Figure 10 shows the robotic fingertip in development at our laboratory.

Conclusion

It wouldn't be an exaggeration to say that every scientific technology is based on sensors. For example, audio recording couldn't exist without the measurement of sound, and television broadcasts would be impossible without catching radio waves as picture signals. Like the human tactile sense, the technology of the developed sensor allows the real-time measurement of complete information about force—that is, direction, magnitude, and distribution. This versatile ability plays a crucial role in our daily lives, even our own identities in space, and we look forward to finding use for high-bandwidth traction sensation in ways yet to be discovered. ■

References

1. R.B. Hetnarski and J. Ignaczak, *Mathematical Theory of Elasticity*, Taylor and Francis, 2004.

2. K. Kamiyama et al., "A Vision-Based Tactile Sensor," *Proc. 11th Int'l Conf. Artificial Reality and Telexistence*, 2001, pp. 127-134.
3. W. Menke, *Geophysical Data Analysis: Discrete Inverse Theory*, Academic Press, 1989.
4. K. Polthier and E. Preu, "Identifying Vector Field Singularities Using a Discrete Hodge Decomposition," *Visualization and Mathematics 3*, Springer-Verlag, 2003, pp. 113-134.



Kazuto Kamiyama is a doctoral student in the Graduate School of Information Science and Technology at the University of Tokyo. His research interests include tactile sensors and virtual reality. Kamiyama received an MS in information science and technology from the University of Tokyo. Contact him at kazuto@star.t.u-tokyo.ac.jp.



Kevin Vlack is a master's student in the Graduate School of Interdisciplinary Information Studies at the University of Tokyo. His research interests include signal processing, computer graphics, and virtual reality. Vlack received a BS in computer science from the College of Engineering at the University of Illinois in Urbana-Champaign. Contact him at vlack@star.t.u-tokyo.ac.jp.



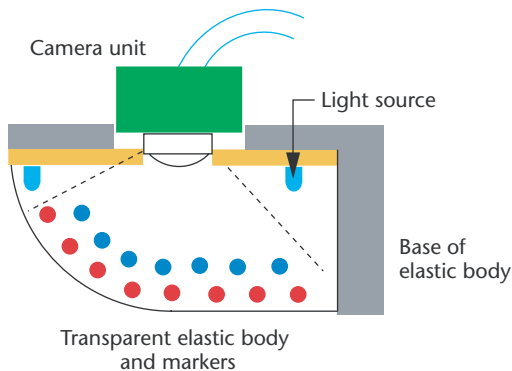
Terukazu Mizota is a researcher in the Department of Information Physics and Computing at the University of Tokyo. His research interests include tactile sensors and virtual reality. Mizota received a BS in general engineering from Tokushima Bunri University. Contact him at mizota@star.t.u-tokyo.ac.jp.



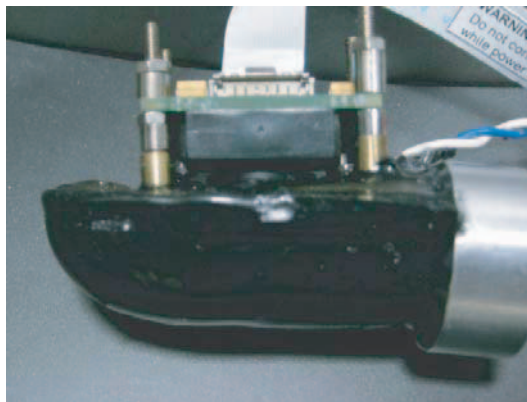
Hiroyuki Kajimoto is a research associate in the Department of Information Physics and Computing at the University of Tokyo. His research interests include tactile displays, tactile sensors, and virtual reality. Hiroyuki received an MS in mathematical engineering and information physics from the University of Tokyo. Contact him at kaji@star.t.u-tokyo.ac.jp.



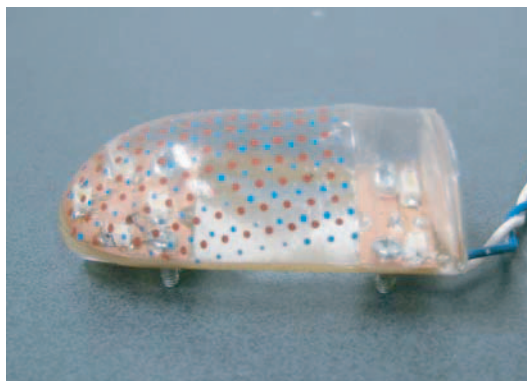
Naoki Kawakami is a lecturer in the Department of Information Physics and Computing at the University of Tokyo. His research interests include virtual reality. Kawakami received a PhD in advanced interdisciplinary studies from the University of Tokyo. Contact him at kawakami@star.t.u-tokyo.ac.jp.



(a)



(b)



(c)



Susumu Tachi is a professor in the Department of Information Physics and Computing at the University of Tokyo. His research interests include virtual reality, psychophysics, and telerobotics. Tachi has a doctoral degree in mechanical engineering from the University of Tokyo. He is a founding director of the Robotics Society of Japan (RSJ), a Fellow of the Society of Instrument and Control Engineers (SICE), and is the founding president of the Virtual Reality Society of Japan (VRSJ). Contact him at tachi@star.t.u-tokyo.ac.jp.

For more on this or any other computing topic, visit our Digital Library at www.computer.org/publications/dlib.

10 Traction field measurement on a robotic finger: (a) basic system schematic, (b) prototype with mounted camera, and (c) finger-shaped elastic body with internal markers.